Celorrio, V., Tiwari, D., & Fermin, D. J. (2016). Composition-dependent reactivity of Ba0.5Sr0.5CoxFe1-xO3- toward the oxygen reduction reaction. *Journal of Physical Chemistry C*, *120*(39), 22291-22297. https://doi.org/10.1021/acs.jpcc.6b04781

Composition-Dependent Reactivity of $Ba_{0.5}Sr_{0.5}Co_xFe_{1-x}O_{3-\delta}$ Towards the Oxygen Reduction Reaction

*Veronica Celorrio, Devendra Tiwari, and David J. Fermin**

School of Chemistry. University of Bristol. Cantocks Close, Bristol, BS8 1TS, United Kingdom

ABSTRACT The electrochemical activity towards the oxygen reduction reaction (ORR) of carbon supported $Ba_{0.5}Sr_{0.5}Co_xFe_{1-x}O_{3-\delta}$ electrodes particles is studied for the first time as a function of chemical composition ($1<x<0$). Highly crystalline $Ba_{0.5}Sr_{0.5}Co_xFe_{1-x}O_{3-\delta}$ particles with the full compositional range were synthesized by an ionic-liquid route, leading to a high degree of phase purity. The structure and composition of the materials were investigated by quantitative XRD and EDX. Electrochemical studies in oxygen-saturated alkaline solutions show that the overall reactivity of the catalyst supported on mesoporous carbon increases as the Co content increases above 50%. DFT calculations, based on the structural parameter obtained from XRD refinements, show that the oxygen-vacancy formation energy decreases as the Co content increases. Oxygen vacancies lead to a higher electron density at the Co atoms, which are identified as the key ORR active sites.

1. INTRODUCTION

$Ba_{0.5}Sr_{0.5}Co_{0.8}Fe_{0.2}O_{3-\delta}$ is a well-studied perovskite material which plays an important role as oxygen reduction catalysts in solid oxide fuel cells[1-3] as well as oxygen permeable membranes.[4, 5] In recent years, several high profile reports have suggested that oxide materials can also be utilized as catalysts for the oxygen evolution (OER) and oxygen reduction reactions (ORR) in alkaline solutions.[6-10] Shao-Horn and co-workers proposed that perovskite materials featuring close to single e_g orbital occupancy exhibit optimum oxygen binding energies for catalyzing these processes.[7] $Ba_{0.5}Sr_{0.5}Co_{0.8}Fe_{0.2}O_{3-\delta}$, commonly referred to as BSCF, fulfills this criterion which was used to rationalize their high OER activity, although later studies have shown that the surface composition of the catalysts is compromised under operational conditions.[11, 12] Fabbri and co-workers evaluated the activity of the same material for ORR, concluding that the activity towards the 4-electron process is relatively modest.[13] This group also reported that ORR activity can be enhanced by preparing composite electrodes with acetylene black carbon, which was rationalized in terms of an increase in the electron density at the Co sites induced by the carbon material.[9, 10] Other studies have suggested that thermal treatment of $Ba_{0.5}Sr_{0.5}Co_{0.8}Fe_{0.2}O_{3-\delta}$ at 950 °C under an oxygen atmosphere leads to activity improvements due to the removal of spinel phases from the surface of the material.[14]

In addition to the e_g orbital occupancy descriptor,[7] the electrocatalytic activity of transition metal oxides have also been described in terms of the whole *d* orbital occupancy[15, 16] and the number of outer electrons.[17, 18] More recently, we have proposed that changes in oxidation state at the B-site in a range close to the formal ORR potential are linked to the high catalytic activity of materials such as Mn-oxides,[19, 20] a view that has also been discussed in other works.[21, 22]

Correlation between catalytic activity and changes of redox state in-operando has also been considered for OER in the case of Ir/Ru oxides[23] and (Ni,Fe)OOH.[24]

In this work, we describe for the first time the activity of $Ba_{0.5}Sr_{0.5}Co_xFe_{1-x}O_{3-\delta}$ particles towards the ORR as a function of the cation ratio in the B-site. In particular, we shall identify the most active B-site composition for the ORR and identify key guiding principles for manipulating the reactivity of these complex materials. Although aspects such as oxygen vacancy formation and migration energies have been correlated with the chemical composition of these materials,[25-28] this report focuses on the room temperature catalytic activity. A route based on ionic liquid/cellulose mixtures is described resulting in the formation of phase pure particles with very high control over composition. Structural parameters such as lattice constants, atomic positions and site occupancies were determined for the different compositions from quantitative analysis of XRD patterns. This structural information was used as basis for calculating oxygen vacancy formation energy (E_{Vo}) under the DFT supercell formalism. We conclude that increasing Co content (x) leads to an increase in the lattice constant of the cell, which is consistent with a lower Co valency and a decrease in E_{Vo}. As the electron density in the Co site increases, particularly in the case of $x > 0.5$, the activity towards ORR increases.

2. EXPERIMENTAL SECTION

$Ba_{0.5}Sr_{0.5}Co_xFe_{1-x}O_{3-\delta}$ powders were synthesized using an ionic liquid/cellulose system.[19, 29, 30] 1 mL of 0.1 M solution was prepared by adding stoichiometric amounts of $Ba(NO_3)_2$ (Sigma-Aldrich), $Sr(NO_3)_2$ (Sigma-Aldrich), $Co(NO_3)_2 \cdot 6H_2O$ (Sigma-Aldrich) and $Fe(NO_3)_3 \cdot 9H_2O$ (Sigma-Aldrich). The solution was then mixed with 1 mL of 1-ethyl-3-methylimidazolium acetate (Sigma), and heated at 80 °C for 3 h. Then, 100 mg of microcrystalline cellulose (10 wt%, Avicel)

was added under strong stirring until a complete dissolution was achieved forming a homogeneous gel (within 1 -2 minutes given the high solubility of cellulose in the ionic liquid). The gel obtained was calcined immediately after preparation in air for 2 h at 950ºC with a 5°C min^{-1} heating rate.

The morphology and composition of the oxides were investigated with scanning electron microscope JEOL SEM 5600 LV with an EDS analyser. EDX mapping was performed with X-max 80 Oxford instruments detector which has a large area sensor operated with high resolution acquisition parameters over large number of pixel (4096) and high dwell time for collection (100 microseconds per pixel). These conditions ensures a good overlap between element distribution and topography. X-ray diffraction patterns were obtained with a Bruker AXS D8 Advance diffractometer featuring a CuKα radiation source (λ = 0.154 nm). Specimens for XRD were prepared by first milling the powder with agate mortar and pestle and then sieving the powder through a 50 μm mesh. The powder were then pressed in PMMA specimen holder with a cylindrical cavity (internal diameter: 25 mm and 1 mm depth), with clean glass slide, for mounting in diffractometer. Quantitative structure refinements were performed on the XRD patterns by the Rietveld method using Fullprof software suite.[31] Pseudo-Voigt functions were used as fitting functions. The thermal parameters were confined to a fixed range, while background polynomial functions were kept up to the sixth order.

Electrodes were prepared by a two-step drop-casting process. Controlled amounts of an ink containing Vulcan and Na^+-exchanged Nafion® (5 wt.%, Sigma-Aldrich) are deposited onto the glassy carbon disk, followed by drop-casting an aqueous suspension of the oxide. Keeping the oxide and carbon in separate suspensions allows visualizing the homogeneity of the suspensions prior to the drop-casting steps. The final loading onto each electrode was 250 μg_{OXIDE} cm^{-2}, 50 μg_{VULCAN} cm^{-2} and 50 μg_{NAFION} cm^{-2}.[19]

Electrochemical measurements were conducted in a three-electrode cell using a rotating ring-disk electrode (RRDE) fitted to an ALS rotation controller and connected to CompactStat bipotentiostat (Ivium). The RRDE electrode consisted of 4 mm glassy carbon disk surrounded by a Pt ring. The collection efficiency was experimentally determined to be 0.4. The electrochemical cell incorporated a Hg/HgO (1 M NaOH, IJ Cambria) placed on a Luggin capillary as reference electrode. To facilitate the discussion, the potentials throughout this work have been quoted versus a RHE. Experiments were carried out at room temperature in 0.1 M KOH saturated with high purity O_2 (BOC). Solutions were prepared with high purity water from a Milli-Q system (≥ 18.2 MΩ).

Ab-initio DFT calculations were performed using the CASTEP code with Generalised Gradient Approximation-Perdew Burke Ernzerhof exchange-correlation functional and pseudopotentials with electronic configurations: Ba ($5s^2$ $5p^6$ $6s^2$), Sr ($4s^2$ $4p^6$ $5s^2$), Co ($3d^8$ $4s^1$), Fe ($3d^7$ $4s^1$), O ($2s^2$ $2p^6$)), have been employed.[32] A 40 atom supercell (expanding the unit cell twice all the three axis) was used with fixed lattice parameter estimated from the XRD quantitative structural refinements. During calculations, a 4x4x4 k-point grid is created under Monkhorst-Pack scheme and the energy cut-off was set to 520 eV. O_2 molecule binding energy and bond length are then calculated to be 5.27 eV and 1.27 Å, respectively, which are close to experimental values of 5.12 eV and 1.29 Å, respectively.[33] Furthermore, formation energies and atomic charges in our study are in good agreement with the values obtained using GGA+U functional for x = 0.8 as reported by Zhang and Bristowe.[34] These results provide an indication of the accuracy of our approach. The ion-charges at the B-site atoms adjacent to the oxygen vacancy centre were calculated using the Bader method.[35]

3. RESULTS AND DISCUSSION

The synthesis of $Ba_{0.5}Sr_{0.5}Co_xFe_{1-x}O_{3-\delta}$ particles was initiated by dissolving appropriate amounts of $Ba(NO_3)_2$, $Sr(NO_3)_2$, $Co(NO_3)_2 \cdot 6H_2O$ and/or $Fe(NO_3)_3 \cdot 9H_2O$ into 1-ethyl-3-methylimidazolium acetate. The metal containing ionic-liquid solution is heated to 80 °C for 3 h, followed by the addition of microcrystalline cellulose to form a gel, which is finally calcined at 950 ºC for 2h. This methodology has been adapted from previous studies targeting the synthesis of phase pure lanthanides.[19, 29, 30] Further details of the synthesis are provided in the Experimental section.

Representative SEM images and EDX mapping of $Ba_{0.5}Sr_{0.5}Co_{0.75}Fe_{0.25}O_{3-\delta}$ are shown in Figure 1. The high resolution SEM image (Figure 1b) shows that the highly corrugated oxide structure is composed of particles in the range of 1 to 2 μm. The elemental mapping displayed in figures 1c-f demonstrates that the composition of the oxides is highly homogenous in the micrometer length scale. Table S1 (supporting information) summarizes the relative metal composition of the particles with respect to the average Ba content as extracted from the EDX analysis over a large ensemble of particles. The elemental ratio largely matches the composition at the precursor solution, confirming the high mixing and oxide conversion efficiency of this method.[29] In the remaining of the discussion, we shall label the various oxides according to the composition estimated by EDX. SEM images in the supporting information (figure S1) shows a similar microstructure for the various oxides. Slightly larger grain sizes are seen in the case of $Ba_{0.5}Sr_{0.5}CoO_{3-\delta}$, however no systematic variations is observed with the oxide composition.

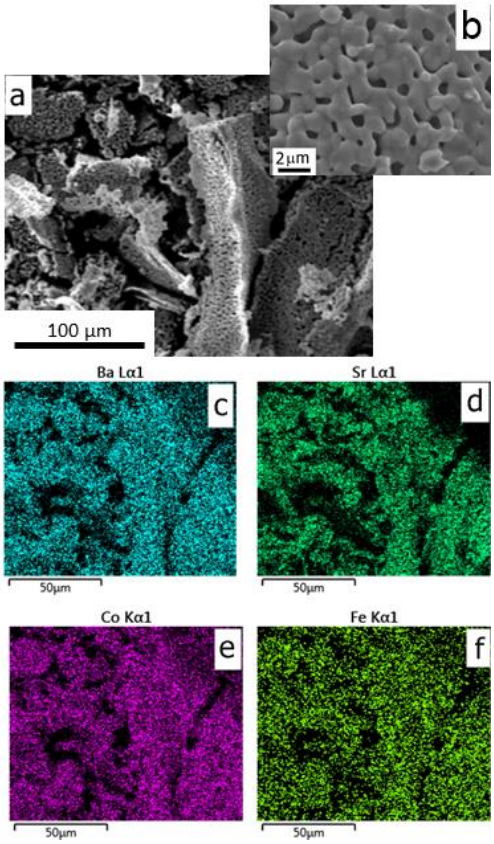

Figure 1. Representative SEM image (a) and high resolution SEM image (b) of $Ba_{0.5}Sr_{0.5}Co_{0.7}Fe_{0.3}O_{3-\delta}$ together with Ba Lα1 (c), Sr Lα1 (d), Co Kα1 (e) and Fe Kα1 (f) elemental mapping shown as colour spots.

X-ray diffraction patterns of the various $Ba_{0.5}Sr_{0.5}Co_xFe_{1-x}O_{3-\delta}$ particles are displayed in Figure 2, which are consistent with a cubic structure (*Pm-3m* space group) for all compositions. The XRD patterns were quantitatively analyzed employing the Rietveld method, revealing a very high degree of phase purity. Details about the XRD analysis, including fitting functions, can be found on the Supporting Information. In agreement with observations by Jung et al.,[14] high phase purity required a crystallization temperature of 950°C. It should be mentioned that hexagonal

phases of BSCF have been reported in the literature, however, the work by Kuklja et al has shown than oxygen vacancies tend to stabilize the cubic phase.[36]

Table 1 contrasts the values of Co content (x) as obtained from EDX and the lattice parameter estimated by XRD refinement. The refined metal occupancies (Table S2) are largely consistent with values obtained from EDX data (Table S1), except for a slight discrepancy for x = 0.70. The excellent quality of the refinement is demonstrated by the statistical correlation coefficients R_p and R_{wp}. The data in Table 1 show a systematic increase in the lattice constant with increasing Co content (x). This trend can be observed more clearly in Figure S2, showing diffractograms in narrow ranges centered at 32^o and 67^o diffraction angles. The peak positions shifts towards larger angles as the Fe content increases. It is also observed that the line width for mixed Co/Fe compositions is broader than the ones consisting only Co or Fe. The variation in line width is associated with slight changes in the mean crystallite sizes between 21 and 45 nm (see table S2). However, the variation in crystallite sizes does no show a correlation with the oxide composition. From these set of experiments, we can conclude that the key structural parameter that systematically changes with the B-site composition is the lattice constant.

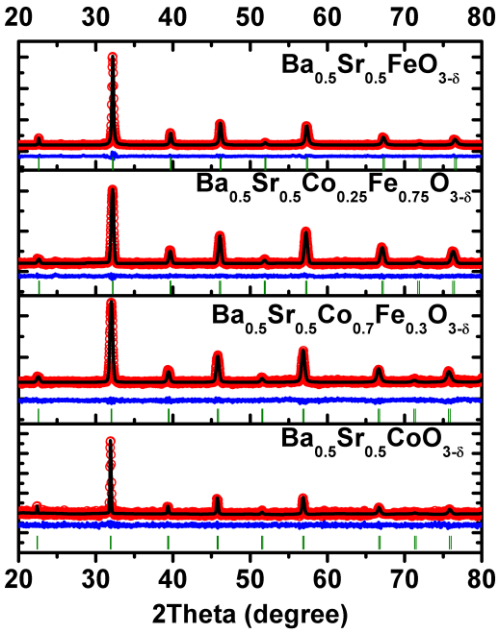

Figure 2. Room temperature X-ray diffraction patterns for $Ba_{0.5}Sr_{0.5}Co_xFe_{1-x}O_{3-\delta}$ calcined at 950°C in air. Red dots correspond to the experimental values while the black thin line corresponds to the Rietveld refinement. The thin blue line shows the difference between experimental and refined patterns. The green bars correspond to the positions of the allowed Bragg reflections for the main phase.

Table 1. Cobalt content as measure by EDX analysis and lattice constant deduced from Rietveld refinement of PXRD data.

Sample	Co content (x)	Lattice Parameter Å
$Ba_{0.5}Sr_{0.5}CoO_{3-\delta}$	1.08 ± 0.16	4.012(3)
$Ba_{0.5}Sr_{0.5}Co_{0.7}Fe_{0.3}O_{3-\delta}$	0.67 ± 0.03	3.991(2)
$Ba_{0.5}Sr_{0.5}Co_{0.25}Fe_{0.75}O_{3-\delta}$	0.20 ± 0.01	3.963(3)
$Ba_{0.5}Sr_{0.5}FeO_{3-\delta}$	-	3.938(5)

The responses obtained for the various oxides supported on a mesoporous carbon film at a rotating ring-disk electrode (RRDE) at 1600 rpm are exemplified in Figure 3. The electrolyte solution was saturated with high purity oxygen with 0.1 M KOH as supporting electrolyte (further details can be found in the experimental section). The responses obtained for the mesoporous carbon layer (Vulcan) are also shown for comparison. The data show that introduction of $Ba_{0.5}Sr_{0.5}Co_xFe_{1-x}O_{3-\delta}$ have little effect on the ORR onset potential with respect to the Vulcan film. It should be mentioned that the onset potentials obtained are within the range of previous works in the literature using BSCF materials.[9, 13, 14] A closer examination of the disk current (i_D) reveals that addition of the oxide particles leads to an increase of the current at potentials above 0.6 V, particularly in the case of $Ba_{0.5}Sr_{0.5}CoO_{3-\delta}$. It can also be seen that the ring current (i_R), which is proportional to the flux of HO_2^- generated at the disk electrode, decreases with respect to the Vulcan electrode in the presence of $Ba_{0.5}Sr_{0.5}CoO_{3-\delta}$. The limiting current does not show a clear plateau at potentials below 0.5 V due to the strong contribution of the Vulcan support. Consequently, the ORR responses involve contributions from the 4-electron process, as well as the two-electron reaction (generating HO_2^-) at the oxide and carbon support.

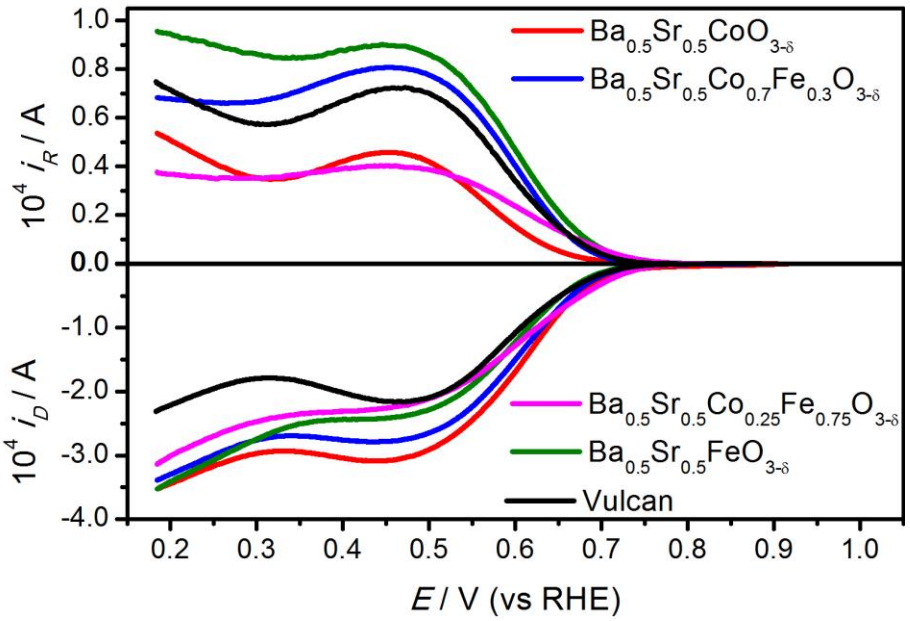

Figure 3. Current-potential curves of Vulcan supported $Ba_{0.5}Sr_{0.5}Co_xFe_{1-x}O_{3-\delta}$ RRDE electrodes at 1600 rpm in O_2-saturated 0.1 M KOH and a scan rate of 10 mV s^{-1}. Pt ring held at a potential of 1.1 V (top panel). The catalyst loading in all samples is 250 μg_{OXIDE} cm^{-2}. Other experimental details can be found in the experimental section.

Figure S2 compares the HO_2^- yields ($X_{HO_2^-}$) and effective number of transferred electrons (n_{e^-}) at 1600 rpm as estimated from the ring and disk currents. The results clearly show that as the Fe content increases, the performance of the catalysts towards the four-electron process substantially decreases. It is also seen that the responses in the presence of $Ba_{0.5}Sr_{0.5}FeO_{3-\delta}$ are very similar to those of the Vulcan support, strongly suggesting that this perovskite is poorly active.

Figure 4a contrasts $X_{HO_2^-}$ and n_{e^-} as a function of the perovskite composition at 0.65 V, as extracted from Figure S3. These results, obtained from averaging the responses of at least three

different samples of each material, clearly show an improvement in activity (above that of Vulcan) for perovskites with high Co content. The kinetic limiting current (i_k) at 0.65 V, as estimated from the dependence of the current on the rotation rate (Koutecky-Levich plots), is shown in figure 4b as a function of the Co content. Characteristic Koutecky-Levich plots for the various materials can be found in the supporting information (Figure S4). The value of i_k (0.65 V) can be regarded as the overall activity of the materials towards the ORR reaction at this potential. We have also extracted the phenomenological electron transfer rate constant for the four electron-step (k_{direct}), based on the Damjanovic model.[37-40] As described in our previous papers,[19, 20] this parameter is dependent of a number of constant including particle size and catalysts loading. Although there is a relatively broad particle size dispersion, this parameter is similar for all of the oxides which is mainly determined by the calcination temperature.

The trends shown in figure 4 consistently show an increase in the activity of the oxide for the overall ORR as well as the direct 4-electron process with increasing content of Co in the B-site, which is more notorious for the high Co content samples. The dotted lines in figure 4b correspond to the values of i_k and k_{direct} measured for the Vulcan support. These data confirm that the electrochemical performance of materials with high Fe content is mainly determined by the carbon support. Previous studies on Sr_2MMoO_6 (M = Fe and Co) have shown that Sr_2CoMoO_6 is more active than Sr_2FeMoO_6, favoring the direct 4-electron pathway.[41] In a previous work, we have also observed that $LaCoO_3$ exhibits slightly higher activity than $LaFeO_3$, although both materials exhibits rate constants orders of magnitude lower than $LaMnO_3$.19 Indeed, kinetically limited currents for $LaMnO_3$ are in the rage of 1-10 A g^{-1},[21] while the pure Co catalyst is close to 0.1 A g^{-1} at 0.65 V. It should be mentioned that the mean particle size of the $Ba_{0.5}Sr_{0.5}Co_xFe_{1-x}O_{3-\delta}$ is more than one order of magnitude higher than those reported for the more active $LaMnO_3$.

Another reason for the higher activity of the Mn based perovskite is the change in redox state of the Mn site at potentials close to the formal ORR potential.[19, 22] Figure S5 contrasts the current-potential characteristics of the various $Ba_{0.5}Sr_{0.5}Co_xFe_{1-x}O_{3-\delta}$ catalysts confirming that no changes in the redox state of Co or Fe sites take place in the relevant potential range.

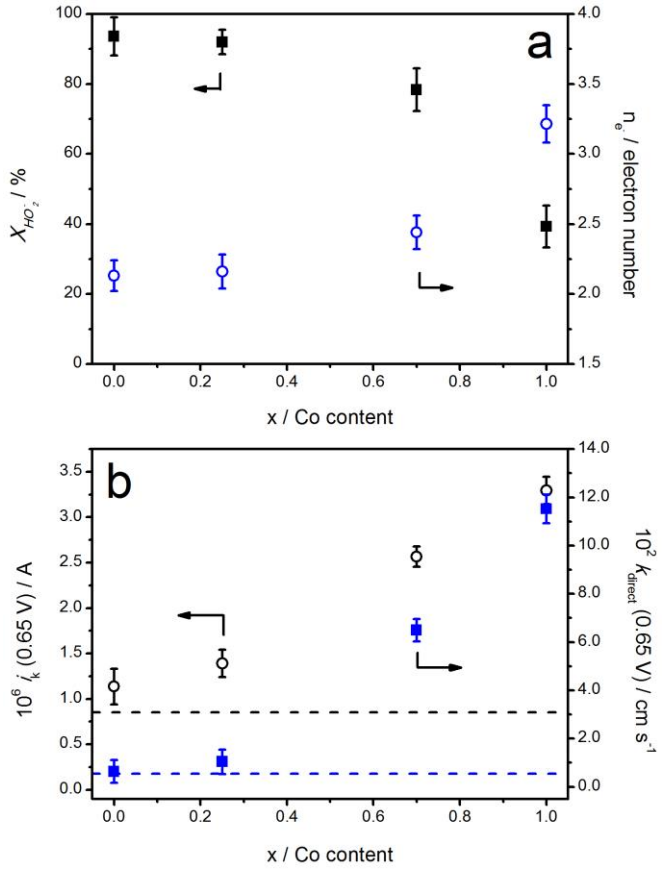

Figure 4. (a) Effective number of transferred electrons (n_e-) reaction and yield of HO_2^- formation during ORR ($X_{HO_2^-}$) at 0.65 V as a function of the Co content as estimated from EDX. (b) Compositional dependence of the kinetic limiting current (i_k) and phenomenological electron transfer rate constant for the 4-electron step (k_{direct}) at 0.65 V vs RHE. The dotted lines correspond to the values of i_k (black) and k_{direct} (blue) measured for the carbon support, i.e. in the absence of oxide particles.

In order to further rationalize the composition dependent activity of the perovskites, oxygen vacancy formation energies (E_{Vo}) were calculated by ab-initio DFT on a 40 atoms supercell schematically shown in figure 5a. The supercells were constructed based on the lattice parameters and atomic positions extracted from the XRD refinement. Functional, pseudopotential and other key information of the calculations are included in the Experimental section. Figure 5b shows the calculated E_{Vo} as a function of the Co content (x). It is observed that E_{Vo} increases with decreasing cobalt content from ~1.2 eV up to 2.3 eV, in agreement with previous theoretical studies of $Ba_{1-x}Sr_xCo_{1-y}Fe_yO_{3-\delta}$.[26, 28] It is interesting to notice that the trend of E_{Vo} correlates with the oxygen occupancy obtained from the XRD refinement (Table S2). E_{Vo} is also calculated in different configurations: when oxygen is removed from in between (i) identical (i.e. FeVoFe and CoVoCo) or (ii) different metal atoms (i.e. FeVoCo). Figure 5b shows that the values of E_{Vo} for different configurations, but the same supercell composition, are very similar, indicating that the electron density is being delocalized over the entire supercell.

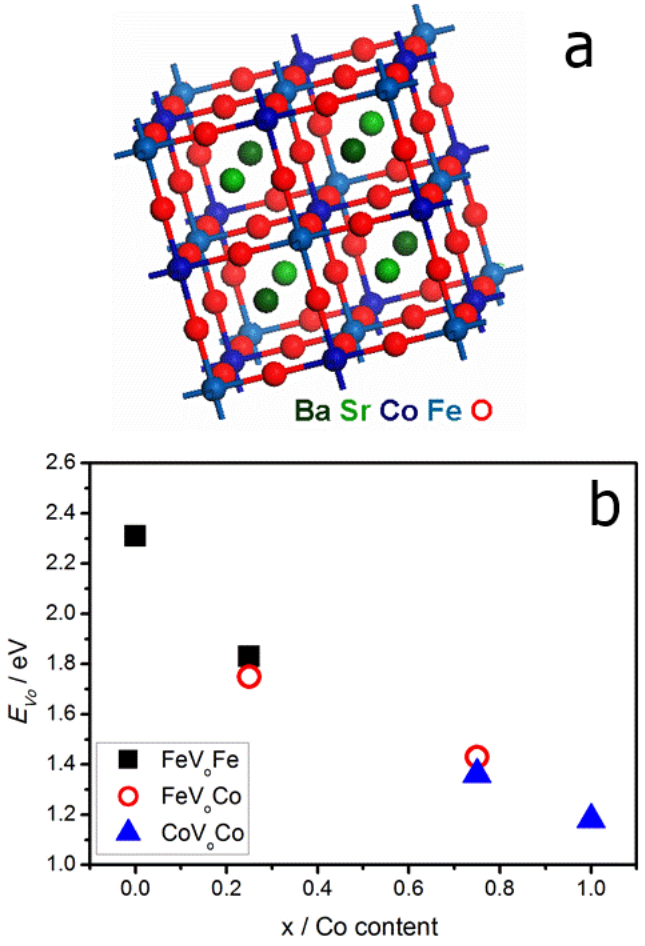

Figure 5. (a) $Ba_{0.5}Sr_{0.5}Co_xFe_{1-x}O_{3-\delta}$ supercell used for calculations. (b) Oxygen vacancy formation energy E_{Vo} as a function of cobalt content (x) in $Ba_{0.5}Sr_{0.5}Co_xFe_{1-x}O_{3-\delta}$.

The effective changes in charge density at a metal site, Δq, as a result of the formation of oxygen vacancies are shown in Table 2. Oxygen vacancy leads to a distribution of the corresponding negative charges onto the nearest transition metal ions (Fe or Co), depending on the configuration. The analysis shows that whenever oxygen is being taken out from a mixed configuration (e.g. FeV_oCo), cobalt acquires a higher share of the charge. It is also observed that the charge on the Co ion decreases as the Co content increases, i.e. a transition from Co^{3+} to Co^{2+}.

Indeed, the work by Merkle et al. has shown that Co exhibits a high density of states near the Fermi level, enabling to adopt lower oxidation states, while Fe orbitals are located above 1 eV higher.[26] XANES studies of $Ba_{0.5}Sr_{0.5}Co_{0.8}Fe_{0.2}O_{3-\delta}$ have shown that the Co oxidation state is between 2^+ and 3^+.[10] As Co^{2+} has a larger ionic radius than Co^{3+} in a six-fold symmetry, the partial reduction of Co^{3+} leads to the expansion of unit cell as observed in the XRD analysis. Furthermore, the strain introduced by the large Ba cation forces the Co ions to adopt a lower oxidation state, and the formation of oxygen vacancies while shifting the Fermi level.[26, 28, 42-44]

Table 2. Oxygen vacancy formation energies (E_{Vo}) and change in charge per atom (Δq) at the neighboring Co or Fe site

X	Configuration	E_{Vo} / eV	Δq_{Co}	Δq_{Fe}
1.00	CoV_oCo	1.18	-0.23	
0.75	FeV_oCo	1.43	-0.25	-0.12
	CoV_oCo	1.36	-0.21	
0.25	FeV_oFe	1.83		-0.15
	FeV_oCo	1.75	-0.17	-0.14
0.00	FeV_oFe	2.31		-0.17

The analysis of E_{Vo} provides various angles for rationalizing the increase of the perovskite ORR activity with Co content. However, we believe that the fundamental link relates to the increase in the electron density at the Co sites as result of oxygen vacancy formation, i.e. the larger the electron density at the Co-sites, the higher is the activity towards ORR. This trend could be

compared to the conclusion reached by Fabbri *et al.*[10] in which the activity of $Ba_{0.5}Sr_{0.5}Co_{0.8}Fe_{0.2}O_{3-\delta}$/carbon composites is improved due to an increase in the electron density at the Co sites promoted by the carbon support. This view appears also consistent with the high activity of Mn based oxides in which the electron density at the catalytic site is directly determined by the electrode potential.[19, 21, 22]

4. CONCLUSIONS

The activity of $Ba_{0.5}Sr_{0.5}Co_xFe_{1-x}O_{3-\delta}$ particles supported at mesoporous carbon electrodes towards the oxygen reduction reaction has been systematically investigated as a function of the B-site composition. Highly phase pure oxide particles with *x* values between 0 and 1 were synthesized with a highly versatile ionic liquid method. Results obtained employing rotating ring-disk electrodes clearly show an increase in the overall ORR kinetics, as well as the direct 4-electron step, as the Co content increases. High Fe-content oxides resulted in activities similar to that of the carbon support.

DFT supported by structural parameters estimated from experimental XRD data, was used to calculate oxygen vacancy formation energies and the associated partial reduction of metal sites. Our results show that the materials with a higher Co content exhibit lower oxygen vacancy formation energy, leading to higher electron density at the Co-site. Towards further improving electrocatalytic performance, the structure of the $Ba_{0.5}Sr_{0.5}CoO_{3-\delta}$/carbon composites requires further optimization, in particular the effective surface area of the oxide phase. As discussed above, the introduction of Ba generates a strain in the lattice which promotes lower oxidation state of Co sites. Systematic studies of the Ba content will also be an interesting strategy to follow, considering the stability arguments discussed in the literature.[36] The picture emerging from this work, as well as our previous studies on Mn containing perovskites,[19, 20] reveals that the ORR activity at these

complex materials appear to improve with increasing electron density at the B-site under operational conditions.

ASSOCIATED CONTENT

Supporting Information. Composition measured by EDX, Rietveld parameters, SEM images, calculation of HO_2^- yield and the number of electrons (n_e) involved in the reaction, Koutecky-Levich plots and Cylic Voltammograms in Ar-saturated 0.1 M KOH solution. This material is available free of charge via the Internet at http://pubs.acs.org.

AUTHOR INFORMATION

Corresponding Author

* E-mail: David.Fermin@bristol.ac.uk

Tel. +44 117 9288981; Fax +44 117 9250612

ACKNOWLEDGMENT

V.C. gratefully acknowledges the UK National Academy and the Royal Society by the support though the Newton International Fellows program. V.C. and D.J.F. are grateful to the financial support by Engineering and Physical Research Council (EPSRC) through the UK Catalysis Hub (grants EP/K014706/1, EP/K014668/1, EP/K014854/1, EP/K014714/1 and EP/M013219/1). D.T. acknowledges the financial support by EPSRC (grant EP/L017792/1). SEM/EDX studies were carried out by the Chemical Imaging Facility at the University of Bristol, with equipments funded by EPSRC under the "Atoms to Applications" grant (EP/K035746/1). DJF is also grateful to the Institute of Advanced Studies of the University of Bristol for the University Research Fellowship

2015. The authors are also indebted to Dr. Laura Calvillo and Prof. Gaetano Granozzi from the University of Padova for their support to this work.

REFERENCES

(1) N.P. Brandon; S. Skinner; Steele, B. C. H. Recent Advances in Materials for Fuel Cells. *Annu. Rev. Mater. Res.* **2003,** *33*, 183-213.
(2) Steele, B. C. H.; Heinzel, A. Materials for Fuel-Cell Technologies. *Nature* **2001,** *414*, 345-352.
(3) Shao, Z.; Haile, S. M. A High-Performance Cathode for the Next Generation of Solid-Oxide Fuel Cells. *Nature* **2004,** *431*, 170-173.
(4) Cao, Z.; Jiang, H.; Luo, H.; Baumann, S.; Meulenberg, W. A.; Voss, H.; Caro, J. Simultaneous Overcome of the Equilibrium Limitations in BSCF Oxygen-Permeable Membrane Reactors: Water Splitting and Methane Coupling. *Catal. Today* **2012,** *193*, 2-7.
(5) Gangopadhayay, S.; Inerbaev, T.; Masunov, A. E.; Altilio, D.; Orlovskaya, N. Structural Characterization Combined with the First Principles Simulations of Barium/Strontium Cobaltite/Ferrite as Promising Material for Solid Oxide Fuel Cells Cathodes and High-Temperature Oxygen Permeation Membranes. *ACS App. Mat. Interfaces* **2009,** *1*, 1512-1519.
(6) Suntivich, J.; Gasteiger, H. A.; Yabuuchi, N.; Nakanishi, H.; Goodenough, J. B.; Shao-Horn, Y. Design Principles for Oxygen-Reduction Activity on Perovskite Oxide Catalysts for Fuel Cells and Metal-Air Batteries. *Nat Chem* **2011,** *3*, 647-651.
(7) Suntivich, J.; May, K. J.; Gasteiger, H. A.; Goodenough, J. B.; Shao-Horn, Y. A Perovskite Oxide Optimized for Oxygen Evolution Catalysis from Molecular Orbital Principles. *Science* **2011,** *334*, 1383-1385.
(8) Risch, M.; Stoerzinger, K. A.; Maruyama, S.; Hong, W. T.; Takeuchi, I.; Shao-Horn, Y. $La_{0.8}Sr_{0.2}MnO_{3-\delta}$ Decorated with $Ba_{0.5}Sr_{0.5}Co_{0.8}Fe_{0.2}O_{3-\delta}$: A Bifunctional Surface for Oxygen Electrocatalysis with Enhanced Stability and Activity. *J. Am. Chem. Soc.* **2014,** *136*, 5229-5232.
(9) Fabbri, E.; Mohamed, R.; Levecque, P.; Conrad, O.; Kötz, R.; Schmidt, T. J. Composite Electrode Boosts the Activity of $Ba_{0.5}Sr_{0.5}Co_{0.8}Fe_{0.2}O_{3-\delta}$ Perovskite and Carbon toward Oxygen Reduction in Alkaline Media. *ACS Catal.* **2014,** *4*, 1061-1070.
(10) Fabbri, E.; Nachtegaal, M.; Cheng, X.; Schmidt, T. J. Superior Bifunctional Electrocatalytic Activity of $Ba_{0.5}Sr_{0.5}Co_{0.8}Fe_{0.2}O_{3-\delta}$/Carbon Composite Electrodes: Insight into the Local Electronic Structure. *Adv. Energ. Mat.* **2015,** *5*, 1402033-1402037.
(11) May, K. J.; Carlton, C. E.; Stoerzinger, K. A.; Risch, M.; Suntivich, J.; Lee, Y.-L.; Grimaud, A.; Shao-Horn, Y. Influence of Oxygen Evolution during Water Oxidation on the Surface of Perovskite Oxide Catalysts. *J. Phys. Chem. Lett.* **2012,** *3*, 3264-3270.
(12) Mohamed, R.; Cheng, X.; Fabbri, E.; Levecque, P.; Kötz, R.; Conrad, O.; Schmidt, T. J. Electrocatalysis of Perovskites: The Influence of Carbon on the Oxygen Evolution Activity. *J. Electrochem. Soc.* **2015,** *162*, F579-F586.
(13) Fabbri, E.; Mohamed, R.; Levecque, P.; Conrad, O.; Kötz, R.; Schmidt, T. J. $Ba_{0.5}Sr_{0.5}Co_{0.8}Fe_{0.2}O_{3-\delta}$ Perovskite Activity towards the Oxygen Reduction Reaction in Alkaline Media. *ChemElectroChem* **2014,** *1*, 338-342.
(14) Jung, J.-I.; Jeong, H. Y.; Kim, M. G.; Nam, G.; Park, J.; Cho, J. Fabrication of $Ba_{0.5}Sr_{0.5}Co_{0.8}Fe_{0.2}O_{3-\delta}$ Catalysts with Enhanced Electrochemical Performance by Removing an Inherent Heterogeneous Surface Film Layer. *Adv. Mater.* **2015,** *27*, 266-271.

(15) Bockris, J. O.; Otagawa, T. Mechanism of Oxygen Evolution on Perovskites. *J. Phys. Chem.* **1983,** *87*, 2960-2971.
(16) Bockris, J. O. M.; Otagawa, T. The Electrocatalysis of Oxygen Evolution on Perovskites. *J. Electrochem. Soc.* **1984,** *131*, 290-302.
(17) Calle-Vallejo, F.; Díaz-Morales, O. A.; Kolb, M. J.; Koper, M. T. M. Why Is Bulk Thermochemistry a Good Descriptor for the Electrocatalytic Activity of Transition Metal Oxides? *ACS Catal.* **2015,** *5*, 869-873.
(18) Calle-Vallejo, F.; Inoglu, N. G.; Su, H.-Y.; Martinez, J. I.; Man, I. C.; Koper, M. T. M.; Kitchin, J. R.; Rossmeisl, J. Number of Outer Electrons as Descriptor for Adsorption Processes on Transition Metals and Their Oxides. *Chem. Sci.* **2013,** *4*, 1245-1249.
(19) Celorrio, V.; Dann, E.; Calvillo, L.; Morgan, D. J.; Hall, S. R.; Fermín, D. J. Oxygen Reduction at Lanthanides: The Role of the B-site. *ChemElectroChem* **2016,** *3*, 283-291.
(20) Celorrio, V.; Calvillo, L.; Dann, E.; Granozzi, G.; Aguadero, A.; Russell, A. E.; Kramer, D.; Fermin, D. J. Oxygen Reduction Reaction at LaxCa1-xMnO3 Nanostructures: Interplay between A-site Segregation and B-site Valency. *Catal. Sci. Tech.* **2016,** doi: 10.1039/C6CY01105E.
(21) Stoerzinger, K. A.; Risch, M.; Han, B.; Shao-Horn, Y. Recent Insights into Manganese Oxides in Catalyzing Oxygen Reduction Kinetics. *ACS Catal.* **2015,** *5*, 6021-6031.
(22) Ryabova, A. S.; Napolskiy, F. S.; Poux, T.; Istomin, S. Y.; Bonnefont, A.; Antipin, D. M.; Baranchikov, A. Y.; Levin, E. E.; Abakumov, A. M.; Kéranguéven, G.; et al. Rationalizing the Influence of the Mn(IV)/Mn(III) Red-Ox Transition on the Electrocatalytic Activity of Manganese Oxides in the Oxygen Reduction Reaction. *Electrochim. Acta* **2016,** *187*, 161-172.
(23) Sardar, K.; Petrucco, E.; Hiley, C. I.; Sharman, J. D. B.; Wells, P. P.; Russell, A. E.; Kashtiban, R. J.; Sloan, J.; Walton, R. I. Water-Splitting Electrocatalysis in Acid Conditions Using Ruthenate-Iridate Pyrochlores. *Angew. Chem. Int. Ed.* **2014,** *53*, 10960-10964.
(24) Friebel, D.; Louie, M. W.; Bajdich, M.; Sanwald, K. E.; Cai, Y.; Wise, A. M.; Cheng, M.-J.; Sokaras, D.; Weng, T.-C.; Alonso-Mori, R.; et al. Identification of Highly Active Fe Sites in (Ni,Fe)OOH for Electrocatalytic Water Splitting. *J. Am. Chem. Soc.* **2015,** *137*, 1305-1313.
(25) Mastrikov, Y. A.; Merkle, R.; Kotomin, E. A.; Kuklja, M. M.; Maier, J. Formation and Migration of Oxygen Vacancies in $La_{1-x}Sr_xCo_{1-y}Fe_yO_{3-\delta}$ Perovskites: Insight from ab initio Calculations and Comparison with $Ba_{1-x}Sr_xCo_{1-y}Fe_yO_{3-\delta}$. *Phys. Chem. Chem. Phys.* **2013,** *15*, 911-918.
(26) Merkle, R.; Mastrikov, Y. A.; Kotomin, E. A.; Kuklja, M. M.; Maier, J. First Principles Calculations of Oxygen Vacancy Formation and Migration in $Ba_{1-x}Sr_xCo_{1-y}Fe_yO_{3-\delta}$ Perovskites. *J. Electrochem. Soc.* **2012,** *159*, B219-B226.
(27) Kotomin, E.; Merkle, R.; Mastrikov, Y.; Kuklja, M. M.; Maier, J. First Principles Modeling of Oxygen Mobility in Perovskite SOFC Cathode and Oxygen Permeation Membrane Materials. *ECS Trans.* **2011,** *35*, 823-830.
(28) Kotomin, E. A.; Mastrikov, Y. A.; Kuklja, M. M.; Merkle, R.; Roytburd, A.; Maier, J. First Principles Calculations of Oxygen Vacancy Formation and Migration in Mixed Conducting $Ba_{0.5}Sr_{0.5}Co_{1-y}Fe_yO_{3-\delta}$ Perovskites. *Solid State Ionics* **2011,** *188*, 1-5.
(29) Green, D. C.; Glatzel, S.; Collins, A. M.; Patil, A. J.; Hall, S. R. A New General Synthetic Strategy for Phase-Pure Complex Functional Materials. *Adv. Mater.* **2012,** *24*, 5767-5772.
(30) Celorrio, V.; Bradley, K.; Weber, O. J.; Hall, S. R.; Fermín, D. J. Photoelectrochemical Properties of $LaFeO_3$ Nanoparticles. *ChemElectroChem* **2014,** *1*, 1667-1671.

(31) Carvajal, J. FULLPROF: A Program for Rietveld Refinement and Pattern Matching Analysis. *Abstracts of the Satellite Meeting on Powder Diffraction of the XV Congress of the IUCr* **1990**.
(32) Perdew, J. P.; Burke, K.; Ernzerhof, M. Generalized Gradient Approximation Made Simple. *Phys. Rev. Lett.* **1996,** *77*, 3865-3868.
(33) NIST Computational Chemistry Comparison and Benchmark Database. *NIST Standard Reference Database Number 101*
(34) Zhang, C.; Bristowe, P. D. First Principles Calculations of Oxygen Vacancy Formation in barium-strontium-cobalt-ferrite. *RSC Adv.* **2013,** *3*, 12267-12274.
(35) Henkelman, G.; Arnaldsson, A.; Jónsson, H. A fast and Robust Algorithm for Bader Decomposition of Charge Density. *Comput. Mater. Sci.* **2006,** *36*, 354-360.
(36) Kuklja, M. M.; Kotomin, E. A.; Merkle, R.; Mastrikov, Y. A.; Maier, J. Combined Theoretical and Experimental Analysis of Processes Determining Cathode Performance in Solid Oxide Fuel Cells. *Phys. Chem. Chem. Phys.* **2013,** *15*, 5443-5471.
(37) Anastasijević, N. A.; Vesović, V.; Adžić, R. R. Determination of the Kinetic Parameters of the Oxygen Reduction Reaction Using the Rotating Ring-Disk Electrode. *J. Electroanal. Chem.* **1987,** *229*, 305-316.
(38) Appleby, A. J.; Savy, M. Kinetics of Oxygen Reduction Reactions Involving Catalytic Decomposition of Hydrogen Peroxide: Application to Porous and Rotating Ring-Disk Electrodes. *J. Electroanal. Chem.* **1978,** *92*, 15-30.
(39) Wroblowa, H. S.; Yen Chi, P.; Razumney, G. Electroreduction of Oxygen: A New Mechanistic Criterion. *J. Electroanal. Chem.* **1976,** *69*, 195-201.
(40) Damjanovic, A.; Genshaw, M. A.; Bockris, J. O.; apos; M. Distinction Between Intermediates Produced in Main and Side Electrodic Reactions. *J. Chem. Phys.* **1966,** *45*, 4057-4059.
(41) Cheriti, M.; Kahoul, A. Double Perovskite Oxides Sr_2MMoO_6 (M=Fe and Co) as Cathode Materials for Oxygen Reduction in Alkaline Medium. *Mater. Res. Bull.* **2012,** *47*, 135-141.
(42) Harvey, A. S.; Litterst, F. J.; Yang, Z.; Rupp, J. L. M.; Infortuna, A.; Gauckler, L. J. Oxidation States of Co and Fe in $Ba_{1-x}Sr_xCo_{1-y}Fe_yO_{3-\delta}$ (x, y = 0.2-0.8) and Oxygen Desorption in the Temperature Range 300-1273 K. *Phys. Chem. Chem. Phys.* **2009,** *11*, 3090-3098.
(43) Arnold, M.; Xu, Q.; Tichelaar, F. D.; Feldhoff, A. Local Charge Disproportion in a High-Performance Perovskite. *Chem. Mater.* **2009,** *21*, 635-640.
(44) Mueller, D. N.; De Souza, R. A.; Brendt, J.; Samuelis, D.; Martin, M. Oxidation States of the Transition Metal Cations in the Highly Nonstoichiometric Perovskite-Type Oxide $Ba_{0.1}Sr_{0.9}Co0.8Fe_{0.2}O_{3-\delta}$. *J. Mater. Chem.* **2009,** *19*, 1960-1963.

TOC Image

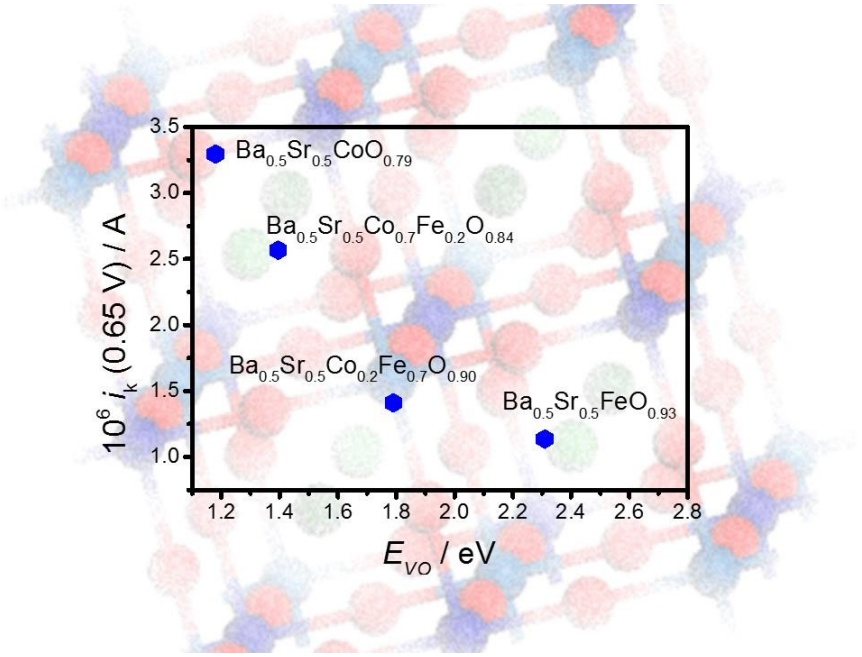
$Ba_{0.5}Sr_{0.5}CoO_{0.79}$
$Ba_{0.5}Sr_{0.5}Co_{0.7}Fe_{0.2}O_{0.84}$
$Ba_{0.5}Sr_{0.5}Co_{0.2}Fe_{0.7}O_{0.90}$
$Ba_{0.5}Sr_{0.5}FeO_{0.93}$
$10^6\ i_k$ (0.65 V) / A
E_{VO} / eV
3.5
3.0
2.5
2.0
1.5
1.0
1.2
1.4
1.6
1.8
2.0
2.2
2.4
2.6
2.8